CrossMark

RESEARCH ARTICLE

Measuring three-dimensional flow structures in the conductive airways using 3D-PTV

Thomas Janke[1] · Rüdiger Schwarze[1] · Katrin Bauer[1]

© Springer-Verlag GmbH Germany 2017

Abstract Detailed information about flow patterns and mass transport in the conductive airways is of crucial interest to improve ventilation strategies as well as targeted drug delivery. Despite a vast number of flow studies in this field, there is still a dearth in experimental data of three-dimensional flow patterns, in particular for the validation of numerical results. Therefore, oscillating flow within a realistic model of the upper human conductive airways is studied here experimentally. The investigated range of Reynolds numbers is $Re = 250$–2000 and the Womersley number is varied between $\alpha = 1.9$–5.1, whereby physiological flow at rest conditions is included. In employing the three-dimensional particle tracking velocimetry measurement technique, we can directly visualize airway specific flow structures as well as examine Lagrangian trajectory statistics, which has not been covered to date. The systematic variation of characteristic flow parameters in combination with the advanced visualization technique sheds new light on the mechanisms of evolving flow patterns. By determining Lagrangian properties such as pathline curvature and torsion, we find that both strongly depend on the Reynolds number. Moreover, the probability density function of the curvature reveals a unique shape for certain flow regions and resembles a turbulent like behavior at the small scales.

1 Introduction

In the past, intense research has been carried out to gain a solid knowledge of the fluid dynamics inside the human airways with the aim of improving the existing ventilation strategies or optimizing drug delivery. One of the earliest experimental investigations on the actual flow behavior inside the upper bronchial tree was conducted by Schroter and Sudlow (1969). They used a simplified representation of the human lung geometry based on data provided by Weibel (1963) and Horsfield and Cumming (1967). With this model, they were able to capture important flow characteristics, like flow separation at bifurcations causing asymmetric flow for inspiration and the development of four-vortex patterns for expiration, generated by flow unification from the previous generations. Since then, continuous effort has been made to build more realistic lung models and to introduce more advanced measurement techniques to this field of research. Nevertheless, there is still a lack of experimental data, which motivated our work. In the following, we want to emphasize our motivation by recapturing some of the most recent research work, while laying our focus on the used models as well as measurement techniques and elaborate, where more work has to be done.

Due to the relatively simple geometry of the Weibel model, it has been investigated excessively. Measurements have been carried out using 1D techniques such as LDA (Kerekes et al. 2016), 2D applications like particle image velocimetry (PIV) (Fresconi and Prasad 2007), as well as magnetic resonance velocimetry (MRV) to reconstruct the whole three-dimensional velocity field (Jalal et al. 2016). Despite the usage of similar geometric models, the applied type of flow is rather different. The work of Kerekes et al. (2016) just covered constant inspiratory flow at a flow rate of 30 l/min, representing breathing under rest conditions.

✉ Thomas Janke
  Thomas.Janke@imfd.tu-freiberg.de

[1] Institut für Mechanik und Fluiddynamik, TU Bergakademie Freiberg, Lampadiusstraße 4, Freiberg, Germany

Fresconi and Prasad (2007) went a step further in investigating steady inspiratory/expiratory as well as oscillatory flow. They carried out a thorough analysis of the developing secondary flow and found a critical Dean number $Dn = 10$, at which noticeable secondary motion starts to occur. In incorporating the time-resolved PIV technique, Ramuzat and Riethmuller (2002) were able to resolve the flow field during the whole breathing cycle (see also Theunissen and Riethmuller 2008). Whereas they just covered the laminar regime (Re <1000), which limits the interpretation of the results to smaller, more distal branches of the conductive airways, the research of Jalal et al. (2016) examined the laminar as well as the turbulent regime with a maximum Reynolds number of $Re = 5000$. One limitation of this research is that they just modeled the steady case of inspiration. However, they showed that the strength of secondary motion reaches a maximum at around $Re = 2000$ and weakens with further increased velocities due to the transition into the turbulent regime. They further found a change of the evolving vortex pattern in the daughter branches with increasing Reynolds numbers.

A next step towards more realistic geometries has been done by Adler and Brücker (2007). They modified the commonly used planar and symmetric models to mimic a more realistic lung by rotating the daughter branches to introduce strong three-dimensional flow as well as incorporating an asymmetric branching of the main bifurcation. The investigated cases covered the flow at rest conditions as well as high-frequency oscillatory ventilation (HFOV). Velocity patterns in various cross sections of the three-dimensional lung model were measured using the particle image velocimetry (PIV) technique.

With increasing performance of medical imaging methods patient specific geometries could be introduced into the research community. Such geometries have been used by Große et al. (2007), Soodt et al. (2013) as well as by Banko et al. (2015). By analogy to the previously described research works, they all differ in the covered flow regimes and employed measurement techniques. Große et al. (2007) conducted their investigations using multi-plane PIV with Reynolds numbers between $Re = 1050$–2100 for oscillatory motion as well as steady-state conditions. Their results emphasize a strong difference between steady-state measurements and oscillatory flow measurements. A further improvement of the multi-plane PIV approach has been done by the use of a scanning stereo PIV system by Soodt et al. (2013). With this quasi-volumetric measurement technique, they were able to reconstruct three-dimensional velocity fields within the trachea and the first bifurcation for laminar and turbulent flow. Yet, the highest achievable Reynolds number ($Re = 2650$) was only investigated for steady inspirational and expirational flow. Only the lower laminar regime has been examined under oscillatory fluid motion.

One of the first true three-dimensional, three-component measurement techniques using a patient specific geometry has been applied by Banko et al. (2015). They used a phased-locked MRV technique to resolve the flow field at a single but recognizable high Reynolds number of $Re = 4200$ with a sinusoidal modeled flow. The investigated model geometry reaches from the mouth down to the fourth bifurcating generation. As a major conclusion, they emphasize that the strength of the secondary flow is strongly dependent on the used geometry and is much higher in the realistic model compared to more simplified ones.

Looking at this brief overview of the most recent research activities, we found that true time-resolved three-dimensional velocity data for oscillatory flow under resting conditions are still missing. To fill this gap, we carry out three-dimensional Particle Tracking Velocity measurements (3D-PTV) to investigate the oscillatory flow ($Re = 250$–2000, α between 1.9 and 5.2) inside a three-dimensional model of the upper human bronchial tree, incorporating six bifurcating generations. With the use of the 3D-PTV technique, we are able to visualize flow features, which have not been reported yet, as well as to derive Lagrangian statistics for particle acceleration, torsion, and curvature. We find that these statistics are giving a new insight to the description of the occurring flow structures and that these can be used as a promising tool to characterize the overall flow inside the human lungs.

2 Methods

2.1 Lung model and flow parameters

For our investigations, we are using a three-dimensional artificial representation of the human lung based on data proposed by Weibel (1963) and Horsfield et al. (1971). The same model has been used in the previous studies (e.g., Adler and Brücker 2007; Bauer et al. 2012; Bauer and Brücker 2015) and has proven its capability of representing important flow structures. For a detailed explanation of the model geometry and its manufacturing, the reader is thus referred to Adler and Brücker (2007) as well as to Ramuzat and Riethmuller (2002). The flow through the lung is modeled as an idealized sinusoidal breathing cycle, parameterized by the breathing frequency f and the tidal volume V_T. For such a flow, the Reynolds number Re and the Womersley number α can be defined as follows:

$$Re = \frac{4 \cdot V_T \cdot f}{d_0 \cdot \nu}, \qquad \alpha = \frac{d_0}{2} \cdot \sqrt{\frac{2 \cdot \pi \cdot f}{\nu}}. \qquad (1)$$

Where d_0 denotes the diameter of the trachea and ν the kinematic viscosity.

We conducted experiments by varying the Reynolds number in a range from $Re = 250$–2000 and the Womersley number between 1.9 and 5.2. For all investigated cases, data were acquired at peak inspiration and expiration phases. For $Re = 2000$ and $\alpha = 3.0$, we additionally measured the flow field at accelerating/decelerating inspiration and expiration phases, respectively, resulting in a total number of six phase positions.

Besides the Reynolds and the Womersley behavior, the Dean number Dn represents an important parameter in denoting secondary flow intensity in curved airway branches, defined by the following:

$$Dn_i = Re_i \cdot \sqrt{\frac{d_i}{2 \cdot r_i}} . \tag{2}$$

The Dean number varies for each branch i and scales with the local Reynolds number, the branch's diameter d_i, as well as the local curvature radius r_i of the model's geometry. All characteristic flow parameters are summarized in Table 1. The indices "L" and "R" at the Dean number refer to the right and left main branch with respect to the anatomical definition.

2.2 Experimental set-up

The key component of the measurement set-up is the model of the human airways, described in Sect. 2.1. The oscillatory motion of the flow is realized by driving a piston diaphragm pump using a linear motor (G400 series, MOOG). The piston motion follows a sinusoidal function with adjustable frequency and amplitude. While the piston's motion frequency directly correlates to the breathing frequency f, the tidal volume V_T can be adjusted by changing the amplitude.

Three high-speed cameras (Phantom V12.1, Vision Research), each equipped with a 50 mm lens (Nikon Nikkor 50 mm/f1.8D), for image recording and three high-power LEDs (PT-121, Luminus Devices) for illumination are used as the imaging system. The camera exposure time was set to 500 μs during which a light-pulse of 450 μs length was flashed. A frame rate of 500 Hz for the cameras and the light sources has been used.

With using a water–glycerin mixture (43:57 mass ratio) as the working fluid, we matched the refractive indices between model and liquid. Polyamide particles (Vestosint) with a mean diameter of $d_p = 100\,\mu m$ were used to seed the flow. These particles are neutrally buoyant, as they have the same density as the liquid. The theoretical Stokes number of these particles can be determined by the following:

$$St = \frac{t_p \cdot u_0}{d_0} = \frac{\rho_p \cdot d_p^2}{18 \cdot \eta_{fl}} \cdot \frac{u_0}{d_0} . \tag{3}$$

This non-dimensional number denotes a ratio of the different time-scales of the solid particles and the fluid flow. For $St \ll 0.01$, the lag-introduced error for particle-based velocity measurements can be assumed to be under 0.7% (Dring 1982). With the particle density $\rho_p = 1150\,kg/m^3$, the fluid's dynamic viscosity $\eta_{fl} = 9.66 \times 10^{-3}\,Pa\,s$, as well as a maximum expected velocity of $u_0 = 2\,m/s$ in the trachea, the resulting Stokes number is $St = 0.0074$. Following the previously given assumption, the slip error of these relatively large particles can still be neglected.

2.3 Three-dimensional particle tracking velocimetry (3D-PTV)

The raw images are evaluated using a three-dimensional particle tracking algorithm. The algorithm is a self-developed code using the MATLAB software package (MATLAB R2015a, Mathworks Inc.) as the developing framework. First tests introducing the code and showing the capability of capturing important flow structures have been presented recently by Janke and Bauer (2016).

The three-dimensional reconstruction of the position of each tracer particle is realized by implementing photogrammetric methods, as presented by Maas et al. (1993). To minimize the occurrence of ghost particles, an iterative particle reconstruction routine has been added. This technique is adapted from the proposed steps by Wieneke (2013).

For the particle tracking itself, a combination of a four-frame search algorithm (Malik and Papantoniou 1993) to initialize particle tracks, and an algorithm incorporating the 'Shake-The-Box' idea (Schanz et al. 2013) for further tracking, is employed.

Due to the cyclic flow nature, we can use an ensemble averaging approach by performing successive measurements at phase-locked positions. With such a technique, we can

Table 1 Overview of the chosen parameters frequency f and tidal volume V_T and their corresponding dimensionless numbers Re, α, and Dn in the right and left main bronchus

f [Hz]	V_T [ml]	Re_0 [−]	α [−]	$Dn_{1,R}$ [−]	$Dn_{1,L}$ [−]
0.06	156	248	1.9	24	19
0.06	313	496	1.9	48	39
0.06	469	744	1.9	71	58
0.15	125	496	3.0	48	39
0.15	250	992	3.0	95	78
0.15	375	1488	3.0	143	116
0.15	500	1984	3.0	190	155
0.30	187	1484	4.3	142	116
0.45	125	1488	5.2	143	116

allow for a lower particle seeding density (ppp ≈ 0.001) but yet yield enough data for an adequate reconstruction.

Each acquired phase ensemble itself represents a small time integration window ($\Delta\varphi = 6/40\,\pi$) during the breathing cycle (see Fig. 1). To take different breathing frequencies into account, while keeping the integration windows comparable, their start and ending point is defined by $\varphi \pm 3/40\,\pi$. Where φ denotes the investigated phase position. Based on the sinusoidal piston motion, inspiration starts at $\varphi = 2/4\,\pi$ with its peak flow at $\varphi = 4/4\,\pi$. Flow reversal occurs at $\varphi = 6/4\,\pi$ and maximum expirational flow is present at $\varphi = 0/4\,\pi$. Accelerating inspiration/expiration is defined to be at $\varphi = 3/4\,\pi$ and $\varphi = 7/4\,\pi$. The decelerating phases are at $\varphi = 5/4\,\pi$ and $\varphi = 1/4\,\pi$, respectively. The size of the integration windows has been chosen arbitrarily to be 7.5% of the whole cycle. Yet, we consider this duration to be short enough to assume a steady state during the time integration.

3 Results and discussion

3.1 Quality of reconstruction

The calibration of the multi-camera system is carried out by traversing a flat checkerboard through the measurement volume. The plate is positioned at six different locations within the measurement volume with a distance of 10 mm
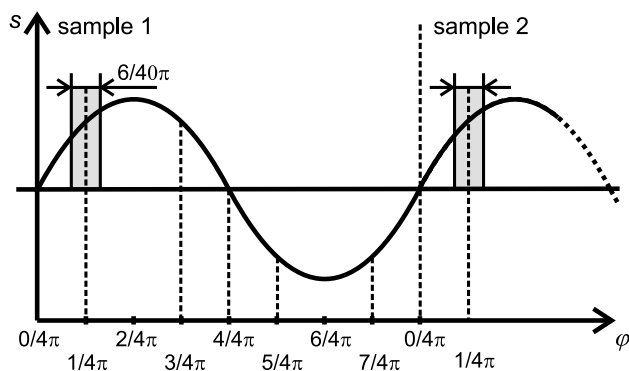

Fig. 1 Piston stroke s over the phase angle φ follows a sinus function. The central positions of the different measurement points for different phase angles φ are marked with a *dashed line*

between each calibration plane. The resulting three-dimensional distribution of calibration points is used to calculate the projection matrix of each camera using a pinhole camera model. Due to practical reasons, the measurements had to be split into four measurement series. Before each measurement series, the calibration was repeated.

The error of reconstruction can be expressed as the difference between the real-image coordinates of each point and the back-projected coordinates of the reconstructed three-dimensional position of this point (Wieneke 2008). This difference is shortly called disparity. The volume averaged disparities after calibration δ_{cal} for each camera and each measurement series are summarized in Table 2.

In addition, the calibration procedure could not be conducted with the lung model being in place. Therefore, the model was removed during the calibration procedure. Due to this fact, reconstruction errors, caused by introducing the model to the light path, cannot be included in the disparity δ_{cal}. To receive a quantification of this influence, the disparity values δ_{run} of around 5000 particles for a representative measurement run within each series have been calculated and averaged. The values are noted in Table 2, as well.

The calibration itself leads to a sub-pixel accurate reconstruction with disparities under 0.3 px. After re-installing the model and calculating the disparities of the reconstructed particles, the error rises up to 2.1 px. Two main reasons are assumed to be responsible for this. On one hand, an inhomogeneous refractive index of the model, caused by the casting process and the aging of the silicone, could be observed. On the other hand, there could be slight shifts in the refractive index of the water–glycerin mixture. Although the refractive index of the liquid was measured regularly, some minor deviations across the whole volume of around 60 l cannot be fully excluded.

An overview over some overall trajectory statistics is given in Table 3. For most of the runs, the reconstructed database consists of around 11,000 trajectories. To minimize the influence of ghost particles/ghost trajectories, only paths with a minimum length greater than five time steps are considered for evaluation. This reduces the number of available trajectories by around 30%. For most cases, the maximum tracked length is over a hundred time steps, while the mean value is at around 20 time steps.

Table 2 Averaged disparity δ of the different measurement series right after the calibration using the calibration points δ_{cal} and calculated with reconstructed particles of an exemplary single measurement run δ_{run}

	δ_{cal} [px]			δ_{run} [px]		
	Cam 1	Cam 2	Cam 3	Cam 1	Cam 2	Cam 3
Measurement series 1	0.16	0.28	0.20	1.75	1.48	1.02
Measurement series 2	0.14	0.17	0.21	1.65	2.13	1.52
Measurement series 3	0.14	0.15	0.17	1.35	1.28	0.91
Measurement series 4	0.10	0.11	0.12	1.29	0.56	0.37
Mean	0.14	0.18	0.18	1.51	1.36	0.96

Table 3 Overall statistics of reconstructed trajectories for maximum inspirational ($\varphi = 4/4\pi$) and expirational flow ($\varphi = 0/4\pi$) at $\alpha = 3.0$, including the total number of reconstructed trajectories n, the number of particle paths tracked for longer than five time steps $n_{>5}$, as well as the averaged track period $\overline{l_{tr}}$, the averaged period $\overline{l_{tr>5}}$ for trajectories tracked for more than five time steps and the maximum period of all particle paths $l_{tr,max}$ as units of the time step dt

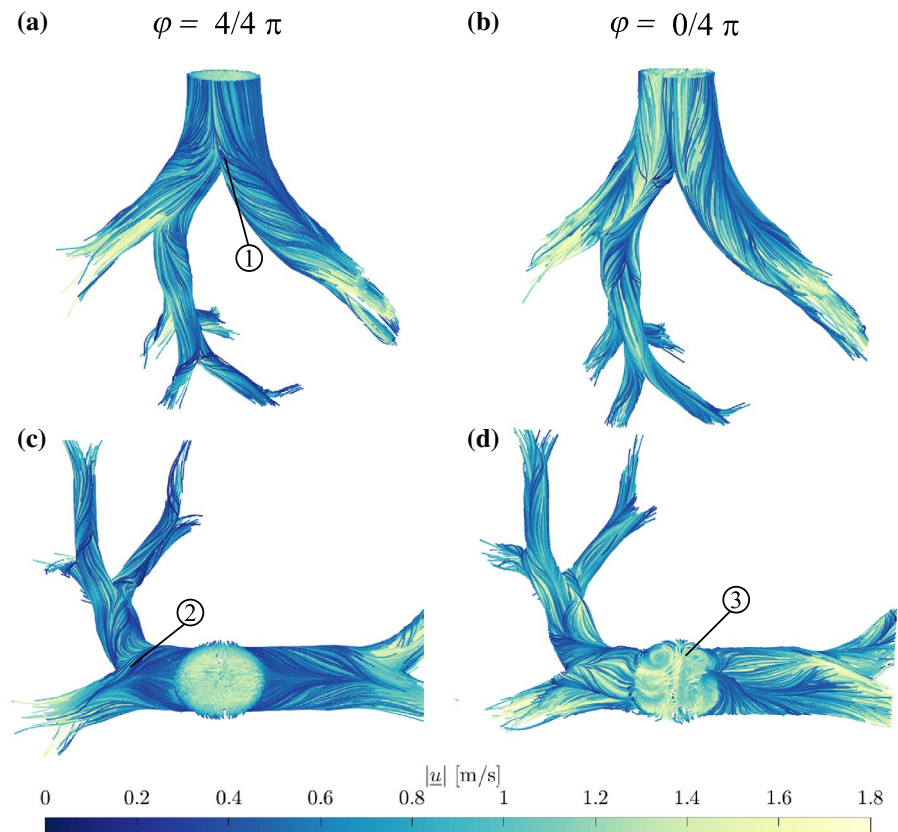| φ	n [−]	$n_{>5}$ [−]	$n_{>5}/n$ [−] (%)	$\overline{l_{tr}}$ [dt]	$\overline{l_{tr>5}}$ [dt]	$l_{tr,max}$ [dt]
Re = 500 α = 3.0						
$4/4\pi$	9420	8335	76	24.98	31.36	124
$0/4\pi$	17,979	7814	71	19.68	25.93	124
Re = 1000 α = 3.0						
$4/4\pi$	9418	8335	79	19.42	23.42	124
$0/4\pi$	12,286	7814	78	18.71	22.74	124
Re = 1500 α = 3.0						
$4/4\pi$	11,288	8640	77	14.57	17.68	109
$0/4\pi$	11,633	8865	76	13.86	16.79	124
Re = 2000 α = 3.0						
$4/4\pi$	11,573	8335	72	11.85	14.74	96
$0/4\pi$	11,074	7814	71	11.59	14.58	152

3.2 Characteristic flow structures

One motivation in using the 3D-PTV approach is to resolve the three-dimensional velocity field while visualizing important flow structures in a very intuitive way by showing actual particle paths.

The typical flow fields for peak inspiration and peak expiration at $Re = 2000$ and $\alpha = 3.0$ are illustrated in Fig. 2. For both cases, the figure provides two different views on the reconstructed volume. For later references, the trachea will also be referred to as G_0, the (anatomical) left main branch as $G_{1,L}$, and the (anatomical) right main branch as $G_{1,R}$, respectively. The results show that we were able to track particles down to the fourth bifurcating generation for a specific region of the model. The particle paths in this figure are color-coded with respect to their local stream-wise velocity. To obtain the velocity information for each line segment, the time derivative of the trajectory's coordinates, using a central differencing scheme, is calculated.

Fig. 2 Reconstructed particle trajectories for $Re = 2000$ and $\alpha = 3.0$ at $\varphi = 4/4\pi$ and $\varphi = 0/4\pi$ *color*-coded with their local stream-wise velocity. **a**, **b** perspective view, **c**, **d** top view

(a) $\varphi = 4/4\pi$　　　　**(b)** $\varphi = 0/4\pi$

(c)　　　　**(d)**

$|\underline{u}|$ [m/s]

0　　0.2　　0.4　　0.6　　0.8　　1　　1.2　　1.4　　1.6　　1.8

For the case of inspiration (Fig. 2a, c), the flow starts to split into the daughter branches already a few millimeters upstream the carina (①). At this point, particle trajectories near the wall start to curl inwards, forming the frequently reported counter-rotating helices (Adler and Brücker 2007; Freitas and Schröder 2008). This structure repeats in every branch, where the symmetry line of the helical pairs changes accordingly to the direction of the model's curvature. Mass being already at the center line seems to be unaffected by the helical motion. Following $G_{1,R}$, it becomes apparent that this strong helical motion can also lead to a cross-flow of near-wall particles towards opposite branches relative to their origin position in the trachea (②). Thus, especially near-wall particles are prone to change their pathway direction, which is crucial for targeted drug delivery.

During expiration (Fig. 2b, d), the typical double vortex pair develops within the tracheal area (③). The evolving helical structure reveals that the influence of distal branches on upstream flow patterns is well preserved. Symmetry line positions of the helix pairs strongly depend on the branching geometry of the daughter branches.

To investigate the flow fields in more detail, Fig. 3 shows three different cuts through the measurement volume at four different phase positions φ (see Fig. 1) during the breathing cycle for $Re = 2000$ and $\alpha = 3.0$. The three cross sections correspond to the trachea, and the right and the left main bronchus, respectively. The color coding is based on a qualitative representation of the local torsion. The torsion τ as well as the curvature κ are two characteristic scalar values to define a three-dimensional curve. Both can be calculated by evaluating the Frenet–Serret formulas. For our case, the curvature and torsion are determined by the following relations:

$$\kappa = \frac{|\underline{\dot{x}} \times \underline{\ddot{x}}|}{|\underline{\dot{x}}|^3} , \tag{4}$$

$$\tau = \frac{\underline{\dot{x}} \cdot (\underline{\ddot{x}} \times \underline{\dddot{x}})}{|\underline{\dot{x}} \times \underline{\ddot{x}}|^2} . \tag{5}$$

In these formulas, $\underline{x}$ is the position vector and time derivatives are marked with a dot. Both scalars have the unit m^{-1}. Mathematically, the curvature can be explained as the deviation of a curve from a straight line and the torsion can be described as a measure of how strong the curve bends away from the plane of curvature. While positive values (red) of torsion indicate a clockwise sense of rotation and negative values (blue) a counter clockwise, respectively.

Overall, we can show that the torsion is suitable in featuring characteristic flow structures, which has been reported in various previous studies (e.g., Ramuzat and Riethmuller 2002; Adler and Brücker 2007; Fresconi and Prasad 2007).

We start with a more detailed analysis by first considering inspiration. Interestingly, while the Dean-type vortices in $G_{1,L}$ (Fig. 3L.a, b) are rather symmetric and capture the whole cross section, as also reported for simplified symmetric model geometries (Fresconi and Prasad 2007; Jalal et al. 2016), the helix pair in $G_{1,R}$ is very small and shifted towards the outer wall (Fig. 3R.a, b), obviously indicating the influence of the next daughter generation.

Fig. 3 Detailed top-to-down view showing reconstructed particle trajectories in different cross sections for $Re = 2000$ and $\alpha = 3.0$, *color*-coded with their local sign of torsion τ at **a** $\varphi = 3/4\,\pi$, **b** $\varphi = 5/4\,\pi$, **c** $\varphi = 7/4\,\pi$ and **d** $\varphi = 1/4\,\pi$. Separation areas are marked with *bold lines*. Dean vortices are highlighted by *dashed circles*
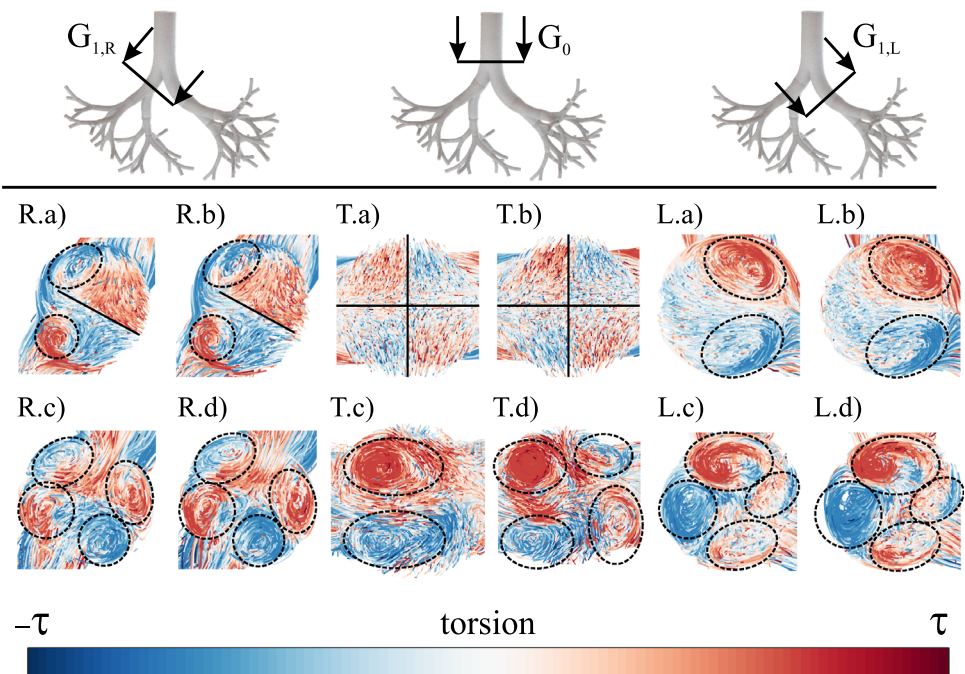
During expiration, we are able to observe a delayed development of the four-vortex pattern inside G_0, which has, to the best of our knowledge, not been reported yet. At the accelerating expiration phase (Fig. 3T.a), only a single helix pair, originating from the right primary bronchus, is detectable. When reaching the state of maximum expiration, an additional pair of helices has developed, forming the typical four-helix pattern (Fig. 2d), which further persists during the deceleration phase (Fig. 3T.d). This difference between acceleration and deceleration suggests that despite the same Reynolds number, the development of certain structures obviously occurs as a certain value of the Reynolds number, and thus, Dean number has been exceeded near the peak velocity phase. Inertia contributes to the enduring existence of the structures during the deceleration phase, although the flow parameters are already below the critical values.

3.3 Influence of Reynolds and Womersley number

Cross sections of the trachea during peak expiration are presented in Fig. 4 to show the influence of different Reynolds Re and the Womersley numbers α. All trajectories are color-coded with the local stream-wise velocity, normalized with respect to the calculated mean velocity u_0 within G_0 used in Eq. (1).

The effect of the Womersley number seems to be negligible, at least in the parameter range investigated here. However, for the different Reynolds numbers, three different regimes can be identified. The first one is a four-vortex structure with a very symmetric arrangement at $Re = 250$. The second pattern is characterized by a single pair of counter-rotating vortices for $250 < Re \leq 1000$ with a high velocity jet in between them. The third structure reveals again the development of two pairs of counter-rotating helices for $Re \geq 1500$ but with a stronger asymmetry compared to the case of $Re = 250$. To our knowledge, such an effect has not been reported yet.

We want to investigate this in further detail by considering the corresponding helicity fields for $Re = 250, 750, 1000, 1500$. The helicity has been calculated by interpolating the Lagrangian velocity vectors onto an equidistant grid using a Gaussian-weighted interpolation (see Fig. 5b). The size of each cell was set to $1.2 \times 1.2 \times 1.2\ \mathrm{mm}^3$. Using this Eulerian representation of the velocity field $\underline{u}$, the helicity H can be calculated for each cell volume V as follows:

$$H = \int_V \underline{u} \cdot (\nabla \times \underline{u})\,\mathrm{d}V. \tag{6}$$

The isosurfaces of the resulting helicity fields, shown in Fig. 5c, envelope values, which are at least $\pm 10\%$ of the maximum calculated helicity. The vortex structures do not change significantly inside the right main bronchus throughout the whole range of Reynolds numbers. This leads to the conclusion that the variation in the emerging vortex pattern

Fig. 4 Detailed top-to-down view showing reconstructed particle trajectories for different Re and α, *color*-coded with their normalized local stream-wise velocity at $\varphi = 0/4\,\pi$. For chosen parameter values, vortices are highlighted for identifying different vortex regimes
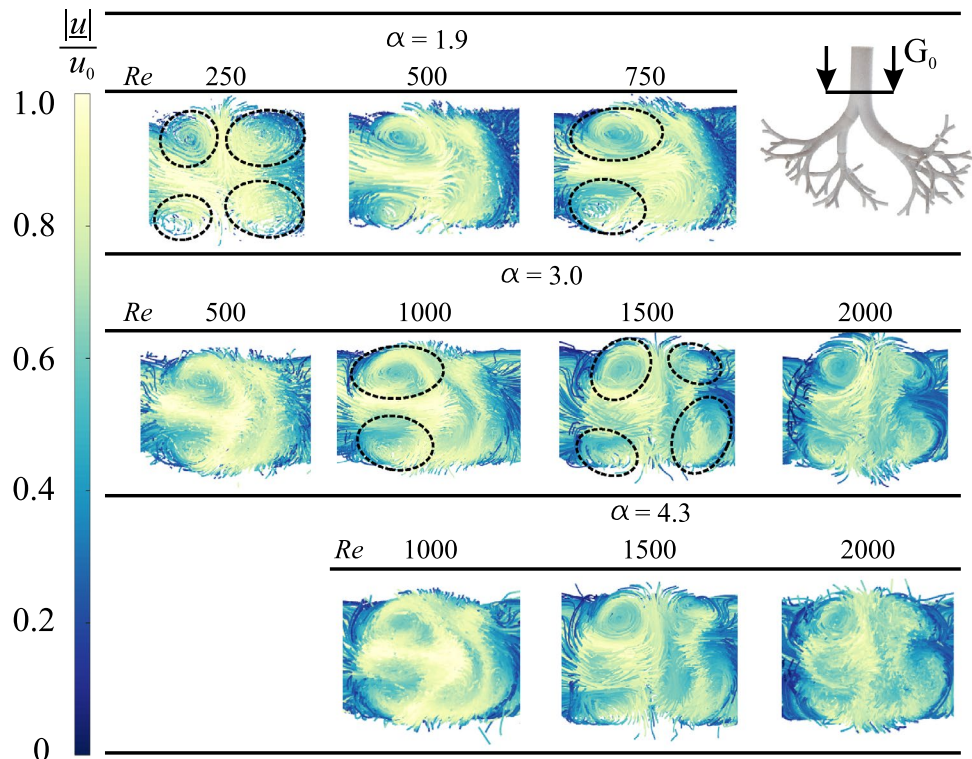
Fig. 5 **a** Measurement volume, in which the helicity H is calculated (*dark gray*). **b** Interpolation of unstructured Lagrangian velocity vectors using a Gaussian-weighted averaging scheme. **c** Isosurfaces of helicity H for $Re = 250$, 750, 1000, 1500 at $\varphi = 0/4\,\pi$ reveal different vortex patterns for different Re. The important vortices in $G_{1,L}$ involved in this development are marked with ①–④
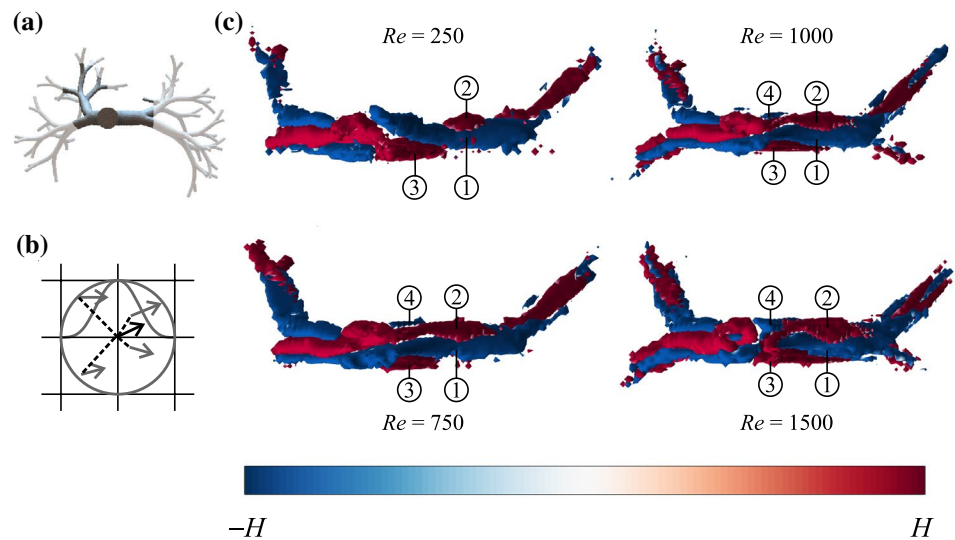
mainly originates from the left branch. Within this section, a large area with negative helicity (①) can be found, starting from the second bifurcation of the model and reaching up to the trachea. This vortex has two partnering counter-rotating vortices (② and ③). The first one (②) is located right after the second bifurcation and rapidly disappears in downstream direction. The second structure (③) develops at around the middle of the bronchus (②). This second structure then builds the fourth observable vortex in the tracheal area. At $Re = 750$, the counter-clockwise rotating vortex (①) is displaced because of a strengthened clockwise rotating vortex (②) originating from the second bifurcation. This displacement leads to a suppression of the former anterior clockwise rotating vortex (③). It is further noticeable that the vortices, sharing the same sense of rotation and originating each from $G_{1,L}$ and $G_{1,R}$, have unified at the main carina. This forms the first observed two-vortex pattern (see Fig. 4, $Re = 750$). At the end of the left main bronchus, a small additional counter-rotating vortex (④) has evolved at the posterior side. This small structure grows in size with further increasing Re and starts to disturb its neighboring vortex (②). At first ($Re = 1000$), with no significant impact, but at $Re = 1500$, it has grown large enough to prevent the unification of the vortices of both branches and starts to reach into the trachea. The very prominent counter-clockwise rotating vortex (①) at the lower Reynolds numbers is now prevented to propagate further and vanishes right at the main carina. At its position, a clockwise rotating vortex (③) can evolve without disturbance and is able to reach up to G_0.

For these mechanisms, the location of the daughter generations in combination with the local Dean number is playing an important role and hence the possibility for the Dean mechanism to develop undisturbed or not. To conclude this section, we found a significant change of the secondary flow structure within this model and could show that the

evolution of the four-vortex structure is quite different for the cases of $Re = 250$ and $Re \geq 1500$ and thus an increasing influence of distal bifurcations on downstream flow patterns at higher Reynolds and Dean numbers, respectively.

3.4 Lagrangian statistics

The 3D-PTV method also offers a new insight to the human lung flow by deriving typical Lagrangian trajectory properties, which are not easily obtainable with Eulerian measurement approaches. One main property is the particle acceleration a, which can be calculated as the second time derivative of the three-dimensional particle path. For the results shown in this subsection, the influence of varying Reynolds number is shown only, since no significant changes could be found by varying the Womersley number. The other two properties which we want to cover are the local torsion and curvature of the particle paths, which we introduced in Sect. 3.2 already.

In Fig. 6, the probability density functions (PDF) of the normalized particle acceleration $a/\sqrt{\overline{a^2}}$ (left) as well as of the normalized local torsion $\tau \cdot d_0$ (right) are given for the area around the main carina (highlighted in dark gray) at different Reynolds numbers during peak inspiration ($\varphi = 4/4\,\pi$). Since no significant differences between the peak inspiration and expiration could be found, results are only presented for peak inspiration.

The shape of the distributions of the local acceleration reveals to be nearly identical for all covered Reynolds numbers. We measure accelerations up to five times the root mean square with a symmetric distribution. In other words, the traced particles experience similar normalized accelerations while passing the airways, independently of the Reynolds number. The average flatness F of all distributions is $F \approx 6.0$. This can be interpreted as a small but noticeable

Fig. 6 PDFs of the normalized local particle acceleration $a/\sqrt{\overline{a^2}}$ (*left*) and the local trajectory torsion $\tau \cdot d_0$ (*right*) within the main carina at peak inspiration $\varphi = 4/4\,\pi$ for different Reynolds numbers. $Re = 250$ ($\square$), $Re = 500$ ($\circ$), $Re = 750$ ($\triangledown$), $Re = 1000$ ($\times$), $Re = 1500$ ($\triangle$), and $Re = 2000$ ($\star$)
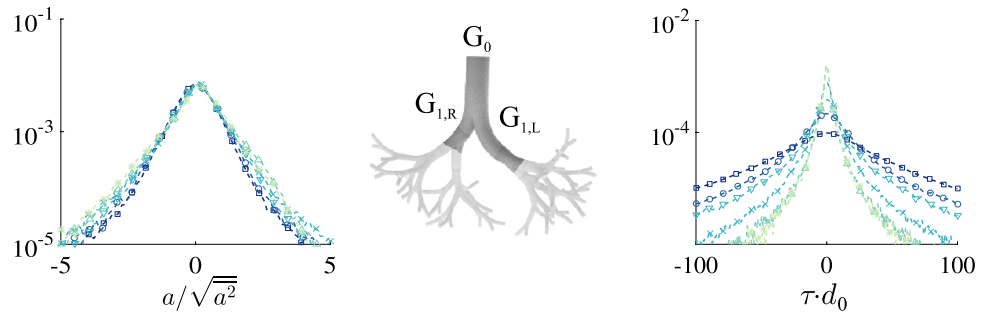
deviation from an idealized Gaussian distribution ($F = 3$). We further calculated the averaged flatness factors for the distribution within $G_{1,L}$ and $G_{1,R}$ separately and received $F_{1,L} = 6.5$ and $F_{1,R} = 4.6$. We can see that the asymmetrical branching leads to differences between those two areas. The acceleration within the right main bronchus tends to follow a more Gaussian distribution. However, note that the Dean number in $G_{1,R}$ is larger than in $G_{1,L}$ with the inverse relation of $Dn_{1,L}/Dn_{1,R} \approx F_{1,R}/F_{1,L} \approx 0.75$. From these results, we can conclude two major findings. On one hand, we find a Reynolds independence of the normalized acceleration PDFs, but we can show that the local geometry of the model has a noticeable impact on the shape of the distribution. On the other hand, we measured acceleration distributions, which deviate from an idealized Gaussian distribution.

In contrast to the particle acceleration, we find a strong Reynolds dependency for the normalized local torsion $\tau \cdot d_0$. With increasing Re, the distributions become narrower. Whereas for lower Re, the probability for larger torsion values increases, resulting in a fat-tail shape. Those larger values indicate a stronger out-of-plane motion from the plane of curvature. As shown in Figs. 2 and 3, most of the particles are following a helical path throughout the airways. With increasing torsion, these helical paths reveal a more elongated shape, probably due to weaker secondary motion at the low Reynolds numbers.

The PDFs for the curvature, normalized with the diameter of the trachea d_0, are presented in Fig. 7 for peak inspiration ($\varphi = 4/4\,\pi$) and for peak expiration ($\varphi = 0/4\,\pi$). We further divide the flow field around the main carina in three sub-areas, covering G_0, $G_{1,R}$, and $G_{1,L}$ separately. Thereby, we find a strong influence of the local geometry on the resulting shape of the PDFs. This becomes especially apparent when comparing the PDFs inside $G_{1,R}$ and $G_{1,L}$ for peak inspiration ($\varphi = 4/4\,\pi$). During this phase, a pair of Dean vortices develops in each of the branches. However, since the length of the left primary bronchus is longer than of the right branch, the developing Dean vortex pair is more prominent in $G_{1,L}$ (see Fig. 3L.b, R.b), although the Dean number is lower in the left branch. A large cross-sectional area is under the influence of these

very symmetric vortices (see Fig. 3L.b). This forces the particles on paths with similar curvature values, resulting in a very sharp peak of the PDF in $G_{1,L}$ for the cases of higher Reynolds numbers. At low Re, however, the PDFs are similar within the primary bronchi, which indicates a less pronounced influence of the airway geometry for the low Reynolds numbers.

During maximum expiration, such a dominant peak cannot be found. Due to the unification of the Dean vortices, originating from the daughter generations, the range of occurring curvatures is broader, which widens the PDFs around the maxima. We can also detect a change of the shape and the location of the maxima in dependency of the Reynolds number. An increasing Re results in a shift of the maximum's location towards smaller $\kappa \cdot d_0$. This means that, at higher Re particle, paths tend to have larger curvature radii. It also becomes apparent that the PDFs converge towards a final shape at $Re = 2000$.

The influence of the local geometry primarily changes the curvature values between $\kappa \cdot d_0 = 0.01{-}1$. The slopes of the distributions for $\kappa \cdot d_0 > 1$ are neither significantly influenced by the geometry nor by the flow phases but only depend on the Reynolds number. This reveals a more universal characteristic of the large curvature values. These slopes can be approximated by a power function with exponents between $-3/2$ for $Re = 250$ and $-5/2$ $Re = 2000$. Such values have been already reported throughout the literature (Xu et al. 2007; Braun et al. 2006; Liberzon et al. 2012), but in the field of turbulence research. The here reported behavior of the curvature PDFs can then be interpreted as an indicator of the slow transition towards the turbulent regime with increasing Re. Or at least, it shows a mimicking behavior of the flow features, resulting in a turbulence like flow mixing at the small scales. In how far this trend develops further for higher Re will be a subject of future investigations. At the larger scales, the cited research works reported a linear slope at the log–log scale, which we are not able to see. This underlines again the influence of the lung geometry on the development of important flow structures, which the cited research works do not represent as they focused on modeling isotropic turbulence.

Fig. 7 PDF of the normalized local trajectory curvature $\kappa \cdot d_0$ in the branches G_0, $G_{1,R}$ and $G_{1,L}$ at peak inspiration $\varphi = 4/4\,\pi$ and peak expiration $\varphi = 0/4\,\pi$ for different Reynolds numbers. $Re = 250$ (□), $Re = 500$ (○), $Re = 750$ (▽), $Re = 1000$ (×), $Re = 1500$ (△), and $Re = 2000$ (⋆)
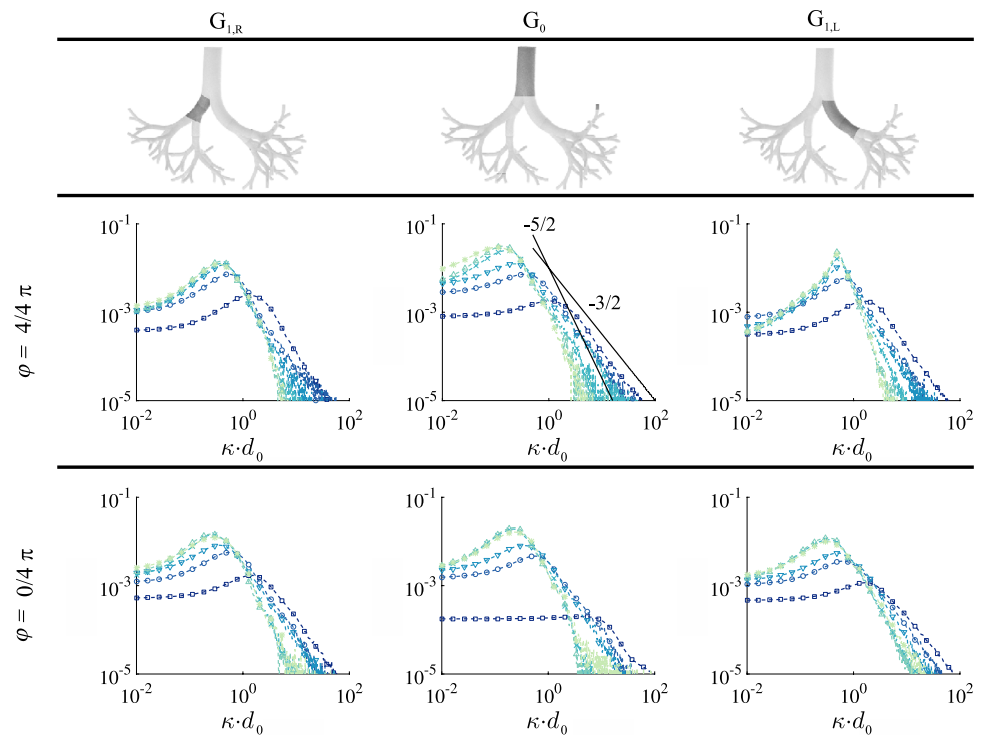
4 Conclusion

The visualization technique of 3D-PTV in the conductive airways allowed us to gain new insights into the three-dimensional nature of helical vortices, which develop in the upper branches of the human bronchial tree. We found that inertia plays a crucial role in maintaining secondary flow structures beyond the peak phases. The systematic variation of characteristic flow parameters revealed an increasing geometric influence of upstream generations on the following branches with increasing Re and Dn, respectively. This influence results in a changing vortex regime between low and high Re during peak expiration. The variation of the frequency, i.e., the Womersley number, does not influence the evolving flow structures.

The 3D-PTV technique further allows to derive characteristic scalars, which can be used to identify flow features, as well as to discuss them in a more general approach by evaluating their corresponding statistics. The analysis of the spatial normalized Lagrangian particle acceleration distribution uncovers a non-Gaussian shape with slightly more pronounced tails, while being independent of the Reynolds number. In contrast to this, we found a Reynolds dependency of the probability density functions for the local torsion and curvature. The curvature results unveil a strong influence of the developing flow field with respect to the local model's geometry at the larger scales. At the small scales, a more universal behavior, following a power-law function with exponents between $-3/2$ and $-5/2$, could be found. This behavior is comparable to the previous studies covering turbulent flow and underlines the good mixing properties of the human lung, even though the flow is not fully turbulent, yet.

In the future, the evaluation of Lagrangian statistics seems to be well suited to compare different lung geometries and their effect on the resulting flow fields without the need of discussing single structures. Moreover, these statistics might be able to reveal an overall systematic of how well certain lung geometries perform with regard to a homogeneous mixing or an optimal drug transport.

References

Adler K, Brücker C (2007) Dynamic flow in a realistic model of the upper human lung airways. Exp Fluids 43(2–3):411–423

Banko AJ, Coletti F, Schiavazzi D, Elkins CJ, Eaton JK (2015) Three-dimensional inspiratory flow in the upper and central human airways. Exp Fluids 56(6):1–12

Bauer K, Brücker C (2015) The influence of airway tree geometry and ventilation frequency on airflow distribution. J Biomech Eng 137(8):081001

Bauer K, Rudert A, Brücker C (2012) Three-dimensional flow patterns in the upper human airways. J Biomech Eng 134(7):071006-1

Braun W, Lillo FDE, Eckhardt B (2006) Geometry of particle paths in turbulent flows. J Turb 7(62):N62

Dring R (1982) Sizing criteria for laser anemometry particles. J Fluids Eng 104(1):15–17

Freitas RK, Schröder W (2008) Numerical investigation of the three-dimensional flow in a human lung model. J Biomech 41:2446–2457

Fresconi FE, Prasad AK (2007) Secondary velocity fields in the conducting airways of the human lung. J Biomech Eng ASME 129(October):722–732

Große S, Schröder W, Klaas M, Klöckner A (2007) Time resolved analysis of steady and oscillating flow in the upper human airways. Exp Fluids 42:955–970

Horsfield K, Cumming G (1967) Angles of branching and diameters of brnches in the human bronchial tree. Bull Math Biophys. 29:245–259

Horsfield K, Dart G, Olson DE, Cumming G (1971) Models of the human bronchial tree. J Appl Physiol 31(2):207–217

Jalal S, Nemes A, Moortele TVD (2016) Three dimensional inspiratory flow in a double bifurcation airway model. Exp Fluids 57(9):1–15

Janke T, Bauer K (2016) Development of a 3D-PTV algorithm for the investigation of characteristic flow structures in the upper human bronchial tree. In: 18th international symposium application laser imaging technology to fluid mechanics

Kerekes A, Nagy A, Veres M, Rigó I, Farkas Á, Czitrovszky A (2016) In vitro and in silico (IVIS) flow characterization in an idealized human airway geometry using laser Doppler anemometry and computational fluid dynamics techniques. Measurement 90:144–150

Liberzon A, Lüthi B, Holzner M, Ott S, Berg J, Mann J (2012) On the structure of acceleration in turbulence. Phys D 241(3):208–215

Maas HG, Gruen A, Papantoniou D (1993) Particle tracking velocimetry in three-dimensional flows Part I Photogrammetric determination of particle coordinates. Exp Fluids 146:133–146

Malik NA, Papantoniou DA (1993) Particle tracking velocimetry in three-dimensional flows Part II : Particle tracking. Exp Fluids 294:279–294

Ramuzat A, Riethmuller ML (2002) PIV Investigation of Oscillating Flows within a 3D Lung Multiple Bifurcations Model. In: 18th Int. Symp. Appl. Laser Imaging Tech. to Fluid Mech

Schanz D, Schröder A, Gesemann S, Michaelis D, Wieneke B (2013) Shake The box: a highly efficient and accurate tomographic particle tracking velocimetry (TOMO-PTV) method using prediction of particle positions. In: 10th international symposium part. image velocimetry

Schroter RC, Sudlow MF (1969) Flow patterns in models of the human bronchial airways. Respir Physiol 7:341–355

Soodt T, Pott D, Klaas M, Schröder W (2013) Analysis of basic flow regimes in a human airway model by stereo-scanning PIV. Exp Fluids 54(6):1562

Theunissen R, Riethmuller ML (2008) Particle image velocimetry in lung bifurcation models. Springer Berlin Heidelberg, Berlin, pp 73–101

Weibel ER (1963) Morphometry of the human lung. Springer, Berlin, Heidelberg

Wieneke B (2008) Volume self-calibration for 3D particle image velocimetry. Exp Fluids 45:549–556

Wieneke B (2013) Iterative reconstruction of volumetric particle distribution. Meas Sci Technol 24(2):024008

Xu H, Ouellette NT, Bodenschatz E (2007) Curvature of Lagrangian trajectories in turbulence. Phys Rev Lett 98(February):1–4